ANNUAL REVIEWS

Annual Review of Nuclear and Particle Science

High-Energy to Ultrahigh-Energy Neutrino Interactions

Mary Hall Reno

Department of Physics and Astronomy, University of Iowa, Iowa City, Iowa, USA; email: mary-hall-reno@uiowa.edu

Annu. Rev. Nucl. Part. Sci. 2023. 73:181–204

First published as a Review in Advance on July 17, 2023

The *Annual Review of Nuclear and Particle Science* is online at nucl.annualreviews.org

https://doi.org/10.1146/annurev-nucl-111422-040200

Keywords

neutrino, neutrino interactions, neutrino astrophysics

Abstract

The cross sections for neutrino interactions with nucleons have been measured directly in accelerator experiments and through the zenith-angle and energy dependence of neutrino events at the IceCube Neutrino Observatory. Fluxes of high-energy neutrinos are produced at the Large Hadron Collider and by cosmic rays in the atmosphere. High-energy neutrinos also come from astrophysical and cosmic sources. The theory of neutrino interactions is reviewed. Current cross-section measurements and prospects for the future are discussed. The focus here is on neutrino interactions for energies larger than 1 TeV.

Contents

1. INTRODUCTION

Neutrinos and antineutrinos, nearly massless neutral particles that experience only weak interactions, appear in nature with energies that range from the eV scale from nuclear reactions in the Sun to 10^{10} GeV and higher energies associated with ultrahigh-energy (UHE) cosmic rays (1). Relic neutrinos that are remnants of the big bang have energies corresponding to their temperature of 1.7 K. Experimental detection of neutrinos from the Sun, from accelerator beams, and from cosmic ray interactions in the atmosphere has revealed a rich structure of neutrino masses and mixing (2).

As neutral particles with only weak interactions, neutrinos are important messengers from energetic astrophysical processes. They can escape astrophysical sources and travel without deflection through environments with magnetic fields to reveal their origins in a way that is complementary to the information carried by cosmic rays and electromagnetic radiation, and now by gravitational waves (3). Along with electromagnetic scattering of electrons, weak scattering of neutrinos and antineutrinos can be used to probe the structure of nucleons and nuclei (4, 5).

Three flavors of neutrinos—ν_e, ν_μ, and ν_τ, each with a corresponding antiparticle—are distinguished by their charged-lepton partner (e, μ, and τ, respectively) produced in charged-current (CC) scattering events. For $E \sim 1$ GeV, for example, the dominant contribution to the ν_μ cross

section with nucleons (protons and neutrons) is $\nu_\mu n \to p\mu^-$ (4, 5). At higher energies, the neutrino cross section is dominated by deep inelastic scattering (DIS), in which neutrinos scatter with the constituents of protons and neutrons and produce additional particles, such as pions. Using beams of neutrinos and antineutrinos generated in proton collisions with nuclear targets, the neutrino and antineutrino cross sections are measured for energies up to ∼360 GeV (6). The best-measured ones are the ν_μ and $\bar{\nu}_\mu$ cross sections. On the other hand, only tens of ν_τ and $\bar{\nu}_\tau$ events have been identified in neutrino beam experiments by signatures of τ decays to yield measurements of the tau neutrino plus antineutrino cross section with large uncertainties (7–10).

Neutrinos are produced in the atmosphere by cosmic ray–air collisions. The weak decays of pions, kaons, and other hadrons produced in these interactions are responsible for the atmospheric neutrino flux (11) that arrives at the surface of Earth and travels to underground detectors. As with neutrino scattering, since weak interactions conserve lepton flavor, the neutrino flavor corresponds to the associated charged (anti-)lepton in a decay, such as $\pi^+ \to \nu_\mu \mu^+$ and $\mu^+ \to \bar{\nu}_\mu e^+ \nu_e$. Absent distinct neutrino masses, the neutrino flavor is conserved in neutrino propagation. Neutrino masses and flavor mixings yield neutrino flavor oscillations, quantum mechanical phenomena that lead to violations of neutrino flavor conservation after neutrino propagation (2, 6). In addition to neutrino mass differences and neutrino flavor mixing angles, neutrino oscillation effects depend on the distance the neutrino propagates (the baseline, L) and the neutrino or antineutrino energy E. There are also oscillation effects associated with neutrino propagation in a dense medium (12). Measurements of atmospheric neutrinos that travel from their production points to distances up to the diameter of the Earth (13), together with experiments that measured the solar neutrino fluxes through a number of interaction channels (14), have yielded a model in which each of the three neutrino flavor states comprises a mix of three mass eigenstates (2, 6). Many current experiments are tuned to optimize L/E for measurements of elements of the neutrino mixing matrix that depend on neutrino flavor mixing angles.

In this review, the focus is on neutrino and antineutrino interactions with $E > 1$ TeV $= 10^3$ GeV, 1 PeV $= 10^6$ GeV, 1 EeV $= 10^9$ GeV, and higher energies. In addition to the atmospheric neutrino flux, high-energy neutrinos are produced in the sources of cosmic rays and by cosmic ray interactions in transit through the Universe. At these high energies, for terrestrial distances L, neutrino oscillation effects are small in the three-flavor model. On the other hand, given our knowledge of neutrino mixing, over astrophysical distances the net effect of neutrino mixing is to wash out the detailed ratios of neutrino flavor production at the source. Instead, approximately equal astrophysical fluxes of each flavor of neutrino arrive at Earth (15–17). Generally, equal numbers of neutrinos and antineutrinos are expected at high energies from astrophysical sources.

As noted, high-energy neutrinos serve important roles as messengers from cosmic accelerators; neutrino interaction measurements test the Standard Model of weak, electromagnetic, and strong interactions and are tools in searches for physics beyond the Standard Model (BSM) (18–21). A crucial ingredient to all of these efforts is the neutrino and antineutrino cross sections, the topic of this review. A summary of the theory of neutrino DIS with nucleons appears in Section 2, followed by a short summary of other Standard Model contributions to the cross section in Section 3. Measurements and future prospects for measurements of the cross sections using astrophysical and atmospheric neutrino sources in the 1-TeV to 10-PeV neutrino energy range are described in Section 4. New experiments that exploit the flux of neutrinos that emerges along the beam pipe direction from high-energy proton–proton collisions at the Large Hadron Collider (LHC) will make neutrino cross-section measurements up to energies of a few TeV (also described in Section 4). Theoretical considerations for neutrino and antineutrino interactions above incident energies of 10 PeV are outlined in Section 5. A brief summary of the work of a number of groups that have developed simulations of UHE neutrino interactions in

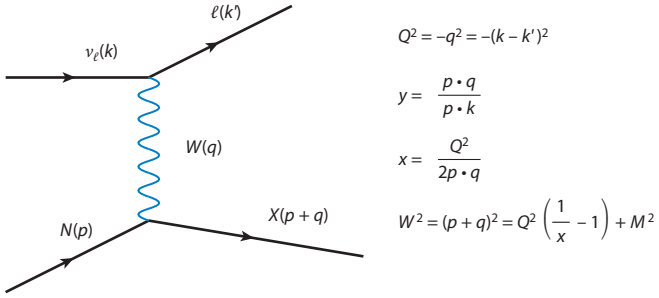

Figure 1

Feynman diagram for neutrino–nucleon charged-current scattering $\nu_\ell(k) + N(p) \to \ell(k') + X(p+q)$ where X is a multiparticle final state. Commonly used variables in inelastic scattering are also shown.

the Earth also appears in Section 5. Prospects for measurements at neutrino and antineutrino energies above 10 PeV are described in Section 6, followed by a summary in Section 7.

2. THEORY OF NEUTRINO DEEP INELASTIC SCATTERING

2.1. Kinematic Variables

This review focuses on the high-energy and UHE inclusive scattering of neutrinos and antineutrinos with nucleons. Neutrinos and antineutrinos can interact with nucleons with the exchange of a charged W boson for CC interactions and with the exchange of a neutral Z boson for neutral-current (NC) interactions. While applicable to both NC and CC scattering, it is convenient to use the CC scattering process $\nu_\ell(k) + N(p) \to \ell(k') + X(p+q)$ for nucleon N and for $\ell = e, \mu, \tau$ to define the kinematic variables since the outgoing lepton ℓ is distinct from the incoming neutrino ν_ℓ. In NC interactions, $\nu_\ell(k) + N(p) \to \nu_\ell(k') + X(p+q)$.

As illustrated in **Figure 1** for ν_ℓ CC scattering, the weak boson carries momentum $q = k - k'$ in a t-channel exchange, so one conventionally works with $Q^2 = -q^2 > 0$. The target nucleon mass is designated $p^2 = M^2$, and the outgoing lepton mass is $(k')^2 = m_\ell^2$. After integrating over all momenta in the hadronic final state, the differential cross section depends on the charged-lepton energy and the direction of its momentum.

The neutrino scattering of interest here occurs in the nucleon target rest frame (lab frame), where the outgoing lepton energy E' is related to the incoming neutrino energy E through the inelasticity y, in the lab frame or equivalently with Lorentz invariant products of four-momenta, written as $y \equiv (p \cdot q)/(p \cdot k) = (E - E')/E$. The lepton angular dependence, defined for θ as the angle between $\vec{k}$ and $\vec{k'}$ in the lab frame, appears through Q^2. In the lab frame, $Q^2 = 4EE'\sin^2\theta/2$ in the high-energy limit ($m_\ell^2 \ll E_\ell^2$). The Bjorken x variable, defined by $x \equiv Q^2/(2p \cdot q)$, combines with y and Q^2 to give $xy(2p \cdot k) = Q^2$. By momentum conservation, the hadronic final-state invariant mass W can be expressed by $W^2 = (p+q)^2 = Q^2(\frac{1}{x} - 1) + M^2$. In terms of the center-of-mass energy squared, $s = (p+k)^2$, the lab-frame energy of the incident neutrino is $E = (s - M^2)/(2M)$. The definitions of these commonly used variables are included in **Figure 1**.

2.2. Neutrino Cross Section with Structure Functions

A particularly useful formulation of the inclusive cross section for neutrino–nucleon scattering, in terms of the variables x and Q^2, or alternatively x and y, is of the form

$$\frac{\mathrm{d}^2\sigma}{\mathrm{d}x\,\mathrm{d}y} = 2xp \cdot k \frac{\mathrm{d}^2\sigma}{\mathrm{d}x\,\mathrm{d}Q^2} = \frac{yG_F^2}{16\pi}\eta_V \left(\frac{M_V^2}{Q^2 + M_V^2}\right)^2 L^{\mu\nu}W_{\mu\nu}. \quad 1.$$

The quantities $L^{\mu\nu}$ and $W_{\mu\nu}$ are the lepton and hadron tensors, respectively, and they are specific to neutrino or antineutrino scattering via vector boson $V = W$ and $V = Z$ exchange for CC and NC scattering, respectively. The constants $\eta_W = 1$ and $\eta_Z = 4$. The leptonic tensor is straightforward to evaluate from the leading-order (LO) diagram in terms of k and k' to get

$$L^{\mu\nu} = 8\Big(k^\mu k'^\nu + k^\nu k'^\mu - k \cdot k' g^{\mu\nu} - i\epsilon^{\mu\nu\alpha\beta} k_\alpha k'_\beta\Big) \qquad 2.$$

for the leptonic contribution to the ν_ℓ CC matrix element squared. The virtual weak boson scattering with the nucleon that includes the sum over all hadronic final states is encoded in $W_{\mu\nu}$. Generically, in terms of the electroweak current of the target nucleon summed over nucleon spins, the hadronic tensor is (22, 23)

$$\begin{aligned} W_{\mu\nu} &\equiv \frac{1}{4\pi} \int \mathrm{d}^4 z e^{iq\cdot z} \langle N | \left[J_\mu(z), J_\nu(0)\right] | N\rangle \\ &= -g_{\mu\nu} F_1 + \frac{p_\mu p_\nu}{p\cdot q} F_2 - i\epsilon_{\mu\nu\rho\sigma} \frac{p^\rho q^\sigma}{2p\cdot q} F_3 \\ &\quad + \frac{2q_\mu q_\nu}{Q^2} F_4 + \frac{p_\mu q_\nu + p_\nu q_\mu}{p\cdot q} F_5 + \frac{p_\mu q_\nu - p_\nu q_\mu}{p\cdot q} F_6. \end{aligned} \qquad 3.$$

The structure functions depend on Q^2 and W^2; however, as discussed below, it is convenient to instead write them as functions of x and Q^2: $F_i = F_i(x, Q^2)$. The structure functions for CC and NC scattering are not the same; the label V for each structure function is suppressed in Equation 3. The structure functions F_i are different for neutrino and antineutrino scattering as well, although at high energies, the neutrino and antineutrino structure functions are essentially equal as described below. Given that the leptonic tensor in Equation 2 depends on only k and k' and that $q = k - k'$, the structure function F_6 cannot contribute to the electroweak LO neutrino scattering cross section.

The tensor contraction $L^{\mu\nu} W_{\mu\nu}$ leads to the differential neutrino (or antineutrino) CC cross section with nucleons. In the differential cross section, F_4 and F_5 multiply powers of m_ℓ^2/s, so in the high-energy limit, contributions from F_4 and F_5 are suppressed. We neglect them here. In the lab frame where $p \cdot k = ME$, the differential cross section for neutrino and antineutrino CC scattering in the high-energy limit is (24)

$$\begin{aligned} \frac{\mathrm{d}^2\sigma^{\nu(\bar\nu)}}{\mathrm{d}x\,\mathrm{d}y} &= \frac{G_F^2 M E_\nu}{\pi(1 + Q^2/M_W^2)^2} \Big(y^2 x F_1(x, Q^2) + (1-y) F_2(x, Q^2) \\ &\quad \pm xy\left(1 - \frac{y}{2}\right) F_3(x, Q^2)\Big), \end{aligned} \qquad 4.$$

where the sign of the F_3 term is positive for neutrinos and negative for antineutrinos. As noted above, the structure functions in Equation 4 are different for ν and $\bar\nu$ scattering; however, the labeling of the structure functions is suppressed in Equation 4. The weak-interaction coupling constant and the W boson mass M_W are combined in the usual way into the Fermi constant G_F. The combination $G_F^2 M/\pi = 1.58 \times 10^{-38}$ cm^2 GeV^{-1} sets the approximate overall scale of the cross section divided by incident neutrino energy E. In the high-energy limit, $0 \le y \le 1$ and $m_\ell^2/(2ME) \lesssim x \le 1$.

As noted above, m_ℓ^2/s corrections are small at high energies and can be neglected for $E > 1$ TeV for the tau neutrino and antineutrino CC cross sections. For reference, in addition to the F_4 and F_5 terms in Equation 3, charged-lepton-mass threshold effects restrict the allowed

kinematic region in the $(x - y)$ plane. Given the differences in structure functions and the sign of the F_3 term for neutrino and antineutrino scattering, the ν_τ and $\bar{\nu}_\tau$ CC cross sections are affected differently by $m_\ell = m_\tau$ corrections. For $E = 100$ GeV, the τ mass corrections reduce the zero-mass CC cross section by ∼6% for $\nu_\tau N$ and ∼26% for $\bar{\nu}_\tau N$, while for $E = 1$ TeV, the τ mass contributions reduce the zero-mass CC cross section by less than 2% for $\nu_\tau N$ and ∼7% for $\bar{\nu}_\tau$ (25). For NC interactions, the final-state lepton is a neutrino, so there are not any mass corrections to the cross section.

2.3. Neutrino Cross Sections in the Massless Parton Model

Decades of experiments that measured inelastic scattering of electron and neutrino beams on nuclear targets and electron–proton beam collisions at HERA have established our understanding of protons and neutrons as being composed of strongly interacting partons: spin-$\frac{1}{2}$ point particles that are quarks and antiquarks, and spin-1 gluons (24, 26–28). Thus, the proton can be treated as a collection of valence quarks (two valence up quarks u and one valence down quark d), gluons, and sea quarks and antiquarks that come from gluon fluctuations $g \to q\bar{q}$.

Gluons do not interact weakly, so to first approximation, neutrinos and antineutrinos interact with quarks and antiquarks. The picture established in electromagnetic and weak DIS analyses is that scattering with nucleons can be treated as the sum of (anti-)lepton–quark and (anti-)lepton–antiquark hard scattering processes where the quark or antiquark momentum is a fraction x_i of the target proton four-momentum, $p_q = x_i p$ (29). The momentum fraction in the massless parton and massless target limit is Bjorken x, $x_i = x$. The parton-level scattering cross sections are weighted by parton distribution functions (PDFs) f_i that depend on x and weakly depend on Q^2. The sum of the weighted cross sections, integrated over x, determines the lepton–nucleon cross section. The structure functions F_i depend on sums of PDFs.

The PDFs, interpreted as determining the probability of a parton in the proton to have momentum fraction x, must satisfy a number of sum rules consistent with the proton having a unit charge and momentum p (24). Approximate isospin symmetry relates the up quark distribution in the proton to the down quark distribution in the neutron. To a very good approximation, the sea quark and sea antiquark distributions are equal for a given quark flavor. Quantum chromodynamics (QCD) effects are responsible for a logarithmic dependence on Q^2 of the PDFs, described by coupled differential equations known as the Dokshitzer–Gribov–Lipatov–Altarelli–Parisi (DGLAP) equations (30–32). Ranges of lepton–hadron and hadron–hadron measurements at different values of (x, Q^2) are translated to consistent sets of PDFs in the framework of the parton model and the DGLAP equations (33, 34).

In what follows, the PDFs are written generically according to the parton label [e.g., $f_u(x, Q^2) = u(x, Q^2) = u$]. For neutrino and antineutrino scattering, we consider scattering from isoscalar nucleon targets—namely, we take the average $(p + n)/2$ using isospin symmetry to relate the neutron PDFs to the proton PDFs.

The weak interactions are structured in families—for instance, for quarks (u, d), (c, s), and (t, b). A feature of CC weak interactions is that the W boson dominantly couples quarks of the same family but also couples between families. The Cabibbo–Kobayashi–Maskawa (CKM) mixing-matrix element $V_{qq'}$ of a three-by-three unitary matrix accounts for the family-diagonal and family-off-diagonal mixing. The CKM matrix is nearly block diagonal; mixing of the first two families dominates and is characterized by an off-diagonal mixing $|V_{us}| \simeq |V_{cd}| \simeq 0.225$ (6). While precision measurements of the CKM matrix elements involving all three families are primary science drivers for lower-energy neutrino experiments, the details of the CKM matrix beyond its nearly block-diagonal structure are less important for the discussion here.

Using CC scattering of neutrinos with quarks $\nu_\ell q \to \ell q'$ and antiquarks $\nu_\ell \bar{q}' \to \ell \bar{q}$ with quark/antiquark momentum p_q as an example, the respective differential cross sections are

$$\frac{d\sigma^{CC}(\nu q)}{dy} = \frac{G_F^2 (k \cdot p_q)^2}{\pi (1 + Q^2/M_W^2)^2} |V_{q'q}|^2, \quad 5.$$

$$\frac{d\sigma^{CC}(\nu \bar{q}')}{dy} = \frac{G_F^2 (k \cdot p_q)^2}{\pi (1 + Q^2/M_W^2)^2} |V_{q'q}|^2 (1 - y)^2. \quad 6.$$

Following the prescription for parton model calculations, the neutrino–quark and neutrino–antiquark scattering cross sections are weighted by the quark and antiquark PDFs and then rearranged to form the structure functions in Equation 4. In the approximation of mixing of four active, massless quarks (u, c, s, and d), the CC structure functions are as follows:

$$F_2^{\nu,CC}(x, Q^2) = 2x(d + s + \bar{u} + \bar{c}) \quad 7.$$

$$F_2^{\bar{\nu},CC}(x, Q^2) = 2x(u + c + \bar{d} + \bar{s}) \quad 8.$$

$$xF_3^{\nu,CC}(x, Q^2) = 2x(d + s - \bar{u} - \bar{c}) \quad 9.$$

$$xF_3^{\bar{\nu},CC}(x, Q^2) = 2x(u + c - \bar{d} - \bar{s}) \quad 10.$$

The CKM mixing-matrix elements do not appear in Equations 7–10 because of the massless-quark approximation and the approximation that the unitary CKM matrix is nearly block diagonal. The NC structure functions for both νN and $\bar{\nu} N$ scattering are

$$F_2^{\nu(\bar{\nu}),NC}(x, Q^2) = \sum_{q=u,d,s,c,b} x(g_{V,q}^2 + g_{A,q}^2)(q + \bar{q}), \quad 11.$$

$$F_3^{\nu(\bar{\nu}),NC}(x, Q^2) = \sum_{q=u,d,s,c,b} 2 g_{V,q} g_{A,q} (q - \bar{q}), \quad 12.$$

in terms of

$$\begin{aligned} g_{V,u} = g_{V,c} = +\tfrac{1}{2} - 2e_u x_W \qquad & g_{A,u} = g_{A,c} = +\tfrac{1}{2} \\ g_{V,d} = g_{V,s} = g_{V,b} = -\tfrac{1}{2} - 2e_d x_W \qquad & g_{A,d} = g_{A,s} = g_{A,b} = -\tfrac{1}{2}, \end{aligned} \quad 13.$$

written with $x_W = \sin^2\theta_W \simeq 0.239$ (6), $e_u = 2/3$, and $e_d = -1/3$. For massless quarks at lowest order in QCD perturbation theory, for both CC and NC interactions, $F_1(x, Q^2)$ is related to $F_2(x, Q^2)$ via the Callan–Gross relation, $2xF_1(x, Q^2) = F_2(x, Q^2)$ (24).

The neutrino and antineutrino CC and NC cross sections divided by energy for scattering with an isoscalar nucleon target as a function of neutrino energy are shown in **Figure 2**. The energy dependence of σ/E shows a characteristic constant behavior at the lower energy range and a decrease in the ratio as the range increases to UHE.

The constant behavior of σ/E near $E = 1$ TeV comes from the fact that the Q^2 dependence of the structure functions and in the prefactor $(M_V^2/(Q^2 + M_V^2))^2$ proportional to the weak boson propagator can be ignored. As **Figure 2** shows, σ/E is approximately constant for $E = 10^3$–10^4 GeV. The growth of the cross section moderates as a function of energy as larger values of Q^2 become important, so σ/E decreases with increasing E. Roughly, $\sigma \sim E^{0.3}$ (35). At high energies,

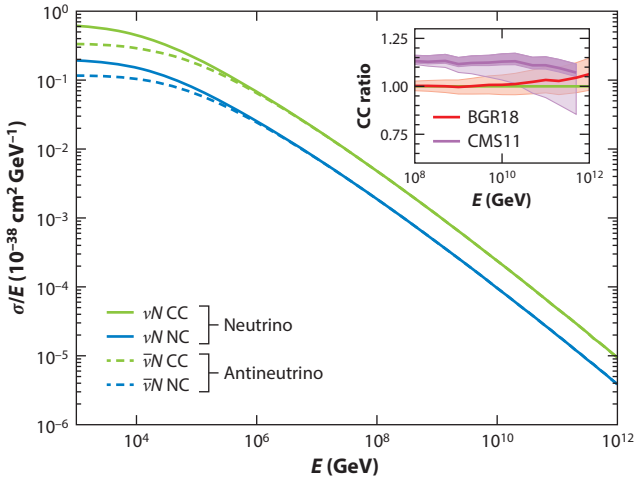

Figure 2

The neutrino (*solid curves*) and antineutrino (*dashed curves*) CC and NC cross sections on isoscalar nucleon targets, divided by energy, as a function of incident neutrino or antineutrino energy E. The cross sections are evaluated at NLO in QCD with the CT18 NLO PDFs (50). The inset shows the CC cross-section ratios relative to the CC cross section shown with the green curve in the figure: for the BGR18 NNLO + NLLx (151) PDFs for the cross section and its PDF error (*red band*) (37) and for the CMS11 NLO cross section (49) with its uncertainty band with (*light purple band*) and without (*dark purple band*) the PDF set that dominates their small-x uncertainty (51) (for further details, see Section 5.1). Inset panel adapted from Reference 37 (CC BY 4.0). Abbreviations: CC, charged current; NC, neutral current; NLO, next-to-leading order; NNLO, next-to-next-to-leading order; NLLx, next-to-leading logarithmic accuracy in $\ln(1/x)$; PDF, parton distribution function; QCD, quantum chromodynamics.

large Q^2 values are accessible. The cross section is suppressed by the V boson propagator as Q^2 increases, but the structure function contributions to σ/E increase at high energies as Q^2 increases. The contribution from the structure function F_2 dominates over the contribution from F_3, and F_2 increases logarithmically in Q^2. Ultimately, the propagator dominates the high-energy behavior, and Q^2 saturates to $\sim M_V^2$, yielding an approximate relation between x, y, and E and $\sim M_V^2$:

$$Q^2 \sim M_V^2 \simeq xy(2ME). \qquad 14.$$

The average inelasticity in neutrino and antineutrino CC and NC scattering is $\langle y \rangle \simeq 0.2$–$0.5$, depending on the energy. At UHE, for both ν and $\bar{\nu}$, $\langle y \rangle \simeq 0.2$ (35). Thus, UHE neutrino and antineutrino scattering probe the small-x behavior of the structure functions, which in turn depend on small-x PDFs.

At small x, the PDFs are dominated by sea quark distributions. In the isospin symmetry limit at small x, the u and d PDFs are $u = \bar{u} = d = \bar{d}$. The charm and strange sea distributions are taken as symmetric between quarks and antiquarks. Altogether, this means that for $E = 10^3$ GeV, where valence quark contributions are important, the ratio of the ν and $\bar{\nu}$ CC cross sections for scattering with nucleons is 1.8, whereas the cross sections are equal at sufficiently high energies where the sea quark distributions dominate. The same ratio for $E = 10^6$ GeV is 1.05 (35, 36). A similar behavior applies to ν and $\bar{\nu}$ NC scattering. In what follows, unless the distinction between neutrinos and antineutrinos is important, the word neutrinos should be understood to include both neutrinos and antineutrinos.

The small-x PDFs are subject to uncertainties because they are out of the kinematic region within which they are extracted from data. PDF analyses use LHC data for $x \gtrsim 10^{-5}$ (6).

Equation 14 indicates that the range of energies relevant to $x \lesssim 10^{-5}$ is $E \gtrsim 10^9$ GeV and, for $x \lesssim 10^{-7}$, $E \gtrsim 10^{11}$ GeV. The approximate relation between the range of x and E is borne out by numeric evaluations of the cross section. For the CC cross section for $E = 10^9$ GeV, ~25% of the cross section comes from $x < 10^{-5}$ (for $E = 10^{11}$ GeV, ~20% comes from $x < 10^{-7}$) (see also Reference 37). More detailed discussions of approaches to small-x structure functions and uncertainties appear in Section 5.1.

The NC cross section for $E \gtrsim 1$ PeV is a nearly constant factor of the CC cross section. For $E = 1$ PeV, the NC/CC cross-section ratio is 0.41, and the ratio increases to ~0.5 at the highest energies shown. The PDF uncertainties for the NC cross section are similar to the uncertainties in the CC cross section since both derive from sea quark contributions at high energies.

2.4. Higher-Order Quantum Chromodynamics Corrections

The structure functions are subject to QCD corrections. Using neutrino CC scattering as an example, at LO in QCD, the parton model contributions to the cross section come from $\nu_\ell q \to \ell q'$ and $\nu_\ell \bar{q}' \to \ell \bar{q}$, for example, with $q = d$ and $q' = u$. Higher-order corrections involve evaluations of processes with more partons in the final state, such as $\nu_\ell d \to \ell u g$ and $\nu_\ell g \to \ell \bar{d} u$. Next-to-leading-order (NLO) corrections introduce the strong coupling constant α_s. The NLO corrections involve $\mathcal{O}(\alpha_s)$ modifications of Equations 7–10 through coefficient functions, thereby also modifying the Callan–Gross relation (24). The DGLAP equations must also be evolved to the appropriate order in α_s. Thus, for formal consistency, the LO cross sections for the parton model evaluation of νN scattering [order $\mathcal{O}(\alpha_s^0)$] are convoluted with the LO PDFs. The NLO result involves α_s corrections to the structure functions and NLO PDFs, and so on. The NLO structure function corrections (38–40) and next-to-next-to-leading-order (NNLO) structure function corrections (41–44) have been known for some time. The corresponding PDFs are available from a number of collaborations; notably, they have been collected in the LHAPDF library (45). The PDFs differ from order to order, but the QCD corrections to the scattering matrix element are not large. For example, using the PDFs from NLO, the ratio of the cross section with NLO structure function corrections to the coefficient functions to LO structure functions evaluated with NLO PDFs is less than 5% (46, 47).

NLO neutrino cross sections by Connolly, Thorne & Waters (CTW) (48), Cooper-Sarkar, Mertsch & Sarkar (CMS11) (49), and Bertone, Gauld & Rojo (BGR18) (37) are frequently used as reference neutrino cross sections. The inset panel in **Figure 2** shows ratios of the CMS11 and BGR18 cross sections relative to the NLO neutrino CC cross section evaluated using the CT18 NLO PDFs (50). The BGR18 CC neutrino–nucleon cross sections are evaluated at NNLO and include additional corrections (discussed in Section 5.1). The NLO CMS11 cross sections are evaluated with HERAPDF1.5 PDFs (51). Error bands from PDF uncertainties are shown.

2.5. Heavy-Flavor Mass Effects

Much theoretical work has focused on quark mass effects in DIS. One approach is to take the u, d, and s as the light quarks in a three-flavor (fixed-flavor) number scheme treatment of the PDFs. Production of c, b, and t and their antiparticles in neutrino and antineutrino scattering is achieved through $2 \to 3$ scattering with a gluon in the initial state (e.g., the virtual W^* scattering $W^* g \to \bar{s} c$ contribution to $\nu_\ell N$ scattering). Kinematic effects associated with the heavy quark masses (generically m_Q) are properly treated (52); however, at high energies and high Q^2, the fixed-flavor number scheme does not benefit from the resummation of large logarithms $\ln(Q^2/m_Q^2)$ that appear. As the energy increases, more quarks have $Q^2 \gg m_Q^2$, and a four- or five-flavor number scheme is more suitable. Variable-flavor number schemes have been introduced that include quark mass effects that effectively interpolate between three-, four-, and five-flavor schemes for light quarks.

The transitions through mass thresholds are implemented with different procedures (53–57). For high-energy neutrino scattering, the only mass that is important is the top quark mass.

The top quark mass of $m_t = 172.5$ GeV suppresses neutrino production of top quarks until $E \gtrsim 10^6$ GeV. One can include the mass through the slow-rescaling prescription. When quark masses are included, the quark momentum fraction does not equal the Bjorken x variable. At LO for $\nu_\ell b \to \ell t$ for b momentum fraction χ, with $M^2 \simeq 0$ and $m_b^2 \simeq 0$, top quark production requires $(q + \chi p)^2 = m_t^2$, so χ is related to Bjorken $x = Q^2/(2p \cdot q)$ (58):

$$\chi = x\left(1 + \frac{m_t^2}{Q^2}\right). \qquad 15.$$

Different implementations of mass effects give b quark–initiated top quark production contributions to the CC cross section in the range of ∼8% to 16% at $E_\nu = 10^{10}$ GeV (59). For NC scattering, the top quark is not produced at LO. At NLO, virtual Z scattering with a gluon $Z^* g \to t\bar{t}$ involves top pair production with a threshold of $4m_t^2$, so it is highly suppressed.

2.6. Nuclear Effects

Measurements of the neutrino and antineutrino cross sections at high energies involve nuclear targets. Whether they are oxygen in water and ice, or tungsten, lead, and argon in neutrino detectors at accelerators, typical targets are not free isoscalar nucleons. A first step to incorporate nuclear effects for a nucleus of mass number A and electric charge Ze is to revise the proton and neutron number,

$$\frac{1}{2}(p + n) \to \frac{1}{A}(Zp + (A - Z)n), \qquad 16.$$

to find the structure functions per nucleon in $\sigma_{\nu(\bar{\nu})A}/A$. This revision affects the cross section in the energy range where the valence contributions are important, $E \lesssim 10^6$ GeV.

Equation 16 does not account for the fact that in the nuclear environment, the PDFs of nucleons are modified. PDFs that are extracted from scattering data with nuclei are labeled nPDFs. Nuclear effects are incorporated directly in the nuclear PDF fit parameters (e.g., as in Reference 60) or as a multiplicative factor to rescale proton PDFs (e.g., as in Reference 61).

Nuclear effects in nPDFs affect regions of x in different ways relative to free proton PDFs (62, 63). For $0.1 < x < 0.2$, an enhancement called antishadowing is seen in the nPDF/PDF ratio, while for $0.2 < x < 0.7$, the so-called EMC effect (64, 65) makes the ratio of the structure function per nucleon F_2 for A and F_2 for N decrease from unity by ∼10–15%, depending on A. Fermi motion increases the structure function ratio for $x > 0.7$. For $x < 0.1$, the main effect is shadowing, an effect that decreases the parton densities in nucleons in nuclei compared with free nucleons. Shadowing is stronger with larger A.

For water targets, the mass-averaged neutrino and antineutrino cross sections are $\lesssim$5% smaller than the cross section with free isoscalar nucleons for $E = 1$ TeV–1 PeV (37). The effect is more important at higher energies. The mass-averaged cross section with water targets is decreased by ∼10% for $E = 10^{12}$ GeV, with estimated uncertainty in the decrease of approximately ±10% (37). An analysis considering the average nucleon number of the Earth of $\langle A \rangle = 31$ shows small nuclear corrections to the cross sections for $E = 1$–10 TeV (59). At UHE, the mass-averaged cross section is also about 10% lower than the free-nucleon cross section, but in this analysis for $\langle A \rangle = 31$, the uncertainty in the ratio of mass-averaged to free-nucleon cross sections ranges between ∼0.8 and 1.15. Nuclear effects can affect the inelasticity distributions, as emphasized in Reference 66, but nuclear corrections to the inelasticity distribution at UHE are expected to be small.

3. OTHER STANDARD MODEL NEUTRINO INTERACTIONS

3.1. Glashow Resonance and Scattering with Atomic Electrons

Neutrinos can scatter with atomic electrons in transit through materials. The largest cross section comes from interactions of high-energy $\bar{\nu}_e$ with atomic electrons to produce an on-shell W^- boson, the so-called Glashow resonance (67). The resonance cross section peaks at $E_{\bar{\nu}_e} = 6.32$ PeV for an electron target at rest. This resonant cross section is a factor of ∼200 times the neutrino–nucleon cross section (68). For hadronic decays of the W^- boson, the full energy of the W^- boson goes into the shower. Evidence for this signature has been seen in the IceCube experiment (69), as briefly reviewed in Section 4.2. For all neutrinos and for $\bar{\nu}_\mu$ and $\bar{\nu}_\tau$, cross sections with atomic electrons at rest are smaller than their cross sections with nucleons. For example, for $E = 6.32$ PeV, the $\nu_\mu e \to \mu \nu_e$ cross section is a factor of ∼1/30 of the $\nu_\mu N$ CC cross section at the same energy (35).

3.2. Subleading Cross Sections

The largest cross section for direct W boson production is through the Glashow resonance, but production of W bosons can also proceed through neutrino scattering with the Coulomb field of a nucleus. For $\nu_\ell A \to \ell^- W^+ A$, the subprocess $\nu_\ell \gamma^* \to \ell^- W^+$ is the dominant process for high-energy scattering with heavy nuclei (70, 71). The cross section scales proportionally to Z^2 for coherent scattering. This can partially compensate for the fact that the $\nu_\ell A \to \ell W^+ A$ is subleading relative to $\nu_\ell A \to \ell X$.

Going beyond using the effective photon approximation, a recent evaluation of the full amplitude squared for $\nu_\ell A \to \ell^- W^+ X$ that includes coherent, diffractive, and incoherent contributions has been performed (72). The cross section divided by incident neutrino energy $\sigma_{\nu A}/E$ is shown for ^{16}O targets in **Figure 3**. At high energies, W boson production by $\nu_e A$ scattering through this process is close to 10% of the DIS cross section at high energy for $A = 16$.

Neutrino-induced trident cross sections are also shown in **Figure 3**. Three leptons can appear in the final state from subprocesses that involve exchanges of Z^0 (labeled NC) or W^+ (labeled CC) that couple to charged and neutral leptons. Through virtual photon exchange from the nucleus to the charged leptons, final states with three leptons arise. **Figure 3** summarizes results for trident production by neutrinos based on leptonic final state.

4. STATUS OF EXISTING MEASUREMENTS AND PROSPECTS FOR 1-TeV TO 10-PeV ENERGIES

4.1. Deep Inelastic Scattering Cross-Section and Inelasticity Measurements

Recent neutrino cross-section measurements by the IceCube Collaboration have exploited the flux of neutrinos produced by cosmic rays in the atmosphere (11) and the diffuse astrophysical fluxes of neutrinos that arrive at Earth from all astrophysical sources (73). The IceCube experiment is a neutrino telescope with 1 km^3 of South Pole ice instrumented to collect the Cherenkov light from showers and muons produced in high-energy neutrino interactions (74). The IceCube experiment has determined that the diffuse astrophysical neutrino flux scales with energy as $\sim E^{-\gamma}$ where the spectral index is $\gamma = 2.37$–2.87 (75, 76). Cross-section measurements by IceCube rely on the cross-section dependence of neutrino flux attenuation through the Earth (77, 78). A key feature is that an increase in neutrino energy decreases the neutrino interaction length $L_\nu(E) = (N_A \sigma)^{-1}$, where N_A is Avogadro's number. Eventually $L_\nu(E)$ becomes shorter than the column depth $X(\theta_z)$, which depends on the zenith angle θ_z. For example, for $\theta_z = 180°$, $L_\nu(E)$ equals the column depth of Earth when $E \simeq 40$ TeV. For $E = 10$ PeV, $L_\nu(E)$ equals the column depth of Earth when $\theta_z \simeq 99°$. As a function of both neutrino energy and zenith angle, Earth absorption effects are markers of

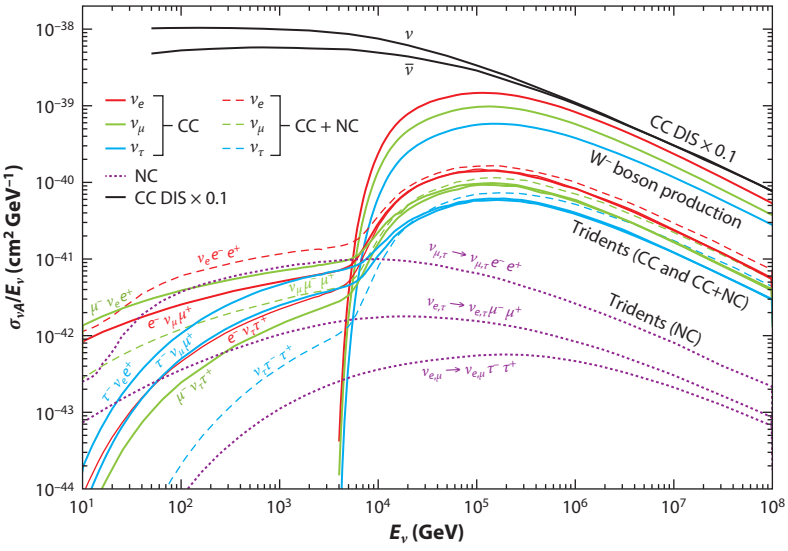

Figure 3

The cross section $\sigma_{\nu A}/E$ as a function of neutrino energy for incident ν_e (*red*), ν_μ (*green*), and ν_τ (*blue*) scattering on oxygen ($A = 16$) for W^- boson and trident production. Trident cross sections, which extend to energies less than 10^3 GeV, are labeled by their leptonic final states for CC (*solid*), CC + NC (*dashed*), and NC (*dotted*) processes. The cross sections for W^- boson production (*solid colored lines*) are nonzero above neutrinos energies of a few TeV. For reference, the black curves show the CC cross section scaled by 0.1 for νA and $\bar{\nu} A$ scattering. Abbreviations: CC, charged current; DIS, deep inelastic scattering; NC, neutral current. Figure adapted from Reference 72 (CC BY 4.0).

the neutrino cross section with nucleons. The number of events depends on the neutrino flux, the neutrino interaction probability proportional to σ, and the attenuation factor that schematically scales as $\exp[-X(\theta_z)/L_\nu(E)]$. This attenuation factor means that signals of neutrinos from below the horizon come from narrower zenith angle ranges (more skimming trajectories) as neutrino energies increase.

The first measurement of the neutrino cross section through Earth absorption effects was performed by the IceCube Collaboration using data from muon neutrino and antineutrino interactions (77). The signals in the detector are muon tracks from CC interactions. Because of the long muon range, the effective volume for muon neutrino interactions is larger than the detector itself, and the angular resolution is less than 0.6° for the energy range of 6.3 to 980 TeV. While the muon energy is known within a factor of two, the incident neutrino energy is part of the modeling of the signal as a function of neutrino cross section. The analysis included fit parameters for several components of the atmospheric flux, the diffuse astrophysical neutrino flux normalization and spectral index, and detector efficiencies. The NC/CC cross-section ratio was assumed to be that of the Standard Model, and the relative cross sections of ν_μ and $\bar{\nu}_\mu$ were fixed as a function of energy. Using 1 year of muon track data, the IceCube analysis yielded a ratio of the measured cross section σ_{meas} to the CMS11 Standard Model cross section σ_{SM} (49) of $1.30^{+0.21}_{-0.19}$ (statistical) $^{+0.39}_{-0.43}$ (systematic) (77). An IceCube analysis of 8 years of muon track data is in progress (79).

All three neutrino flavors contribute to high-energy showers that start in the IceCube detector, the so-called high-energy starting events (HESEs). Contributions come from NC interactions and from ν_e, $\bar{\nu}_e$, ν_τ, and $\bar{\nu}_\tau$ CC interactions. An advantage in the HESE data analysis is that the shower energy in the event is more directly tied to the neutrino energy; however, the zenith

angle resolution is of order 15°. Again, the ratio of NC/CC cross sections is fixed to the Standard Model values, and the CC cross section is represented by a scaling of σ_{SM} of Reference 49. The IceCube analyses of 7.5 years of HESE IceCube data with neutrino energy bins that cover the range 60 TeV–10 PeV (78) and the analysis of HESE data for the energy range 18 TeV–2 PeV (80) yield neutrino cross-section measurements consistent with the Standard Model but with larger uncertainties than for the corresponding muon track analysis.

The IceCube Collaboration has performed an analysis to reconstruct the inelasticity y from neutrino interactions. IceCube finds the average inelasticity for five energy bins in the neutrino energy range of 1.5 to 340 TeV. The combined ν_μ and $\bar{\nu}_\mu$ CC average inelasticities in each energy bin are consistent with the Standard Model (81, 82).

There are prospects for neutrino cross-section measurements from neutrino telescopes in water. One feature of optical Cherenkov detectors in water is that the angular resolutions are better than in ice, an advantage in measuring θ_z in cross-section analyses. KM3NeT (83), a successor to the ANTARES neutrino telescope (84), is a project with two Cherenkov telescopes with optical modules of photomultipliers, set in two locations deep (2.5–3.5 km below the surface) in the Mediterranean Sea. The Oscillation Research with Cosmics in the Abyss (ORCA) detector targets neutrino oscillation physics in the 1- to 100-GeV range, while the Astroparticle Research with Cosmics in the Abyss (ARCA) telescope is designed for the energy range of 100 GeV to 100 PeV. The detection units constituted by strings of digital optical modules are being installed on a phased schedule, with anticipated completion of installation of infrastructure in 2027 for ARCA. ARCA's angular resolution for the reconstructed neutrino direction from tracklike events is ∼0.1° for $E_\nu > 100$ TeV. Shower-like events yield an angular resolution of the neutrino direction that is better than a few degrees.

The Baikal Gigaton Volume Detector (Baikal-GVD) (85), a Cherenkov neutrino telescope, has been operating with detector strings anchored at a depth of 1,366 to 1,367 m in Lake Baikal (Russia) since 2016. Currently with an instrumented volume of ∼0.4 km^3, the effective volume will increase to a cubic kilometer by 2025.

The Pacific Ocean Neutrino Experiment (P-ONE) initiative (86) would use the existing ocean observatory infrastructure off the coast of Canada to construct a multicubic-kilometer Cherenkov neutrino telescope. Work has been undertaken to determine optical properties and light backgrounds of the location, and a prototype string is under development (87).

4.2. Glashow Resonance

The IceCube Collaboration reported evidence of a Glashow resonance event with a shower energy of 6.05 ± 0.72 PeV (69), consistent with $\bar{\nu}_e e \to W \to$ hadrons. The central value of the shower energy is less than 6.32 PeV; however, not all of the particles in the hadronic shower produce detectable Cherenkov radiation. This single event is in the context of 1.55 expected events (69). Additional signatures of the Glashow resonance from the $W \to \mu\bar{\nu}_\mu$ and $W \to \tau\bar{\nu}_\tau$ decay channels may expand the sample size (88).

4.3. FASERν, AdvSND, and a Forward Physics Facility

Accelerator neutrino beams from hadrons incident on fixed targets do not yield neutrinos with energies in the TeV energy region; however, in hadron colliders, neutrinos are copiously produced from hadron production and decay along the direction of the beam pipe (89, 90). Two experiments, FASERν (91) and SND@LHC (92), were installed and commissioned in 2022 for the start of Run 3 at the LHC with a center-of-mass energy of $\sqrt{s} = 13.6$ TeV. The detectors are in existing service tunnels; FASERν is along the collision axis line of sight and SND@LHC is slightly off axis, and

each one is 480 m from the interaction point of the ATLAS experiment and shielded by ∼100 m of rock and concrete.

The FASERν experiment has a tungsten target mass of 1.1 tonnes and uses emulsion detectors and a veto station. It has a silicon tracker between FASERν and its companion experiment's (i.e., FASER's) spectrometer. The SND@LHC experiment has a hybrid detector with an 830-kg target made of tungsten plates, emulsion detectors, electronic trackers, and a muon system. Together, for LHC Run 3 with an integrated luminosity of 150 fb^{-1} and a neutrino plus antineutrino flux that extends to ∼2–4 TeV, approximately 12,000 flavor-tagged CC neutrino interactions will be accumulated, and of order 20 tau neutrino and antineutrino events will be accumulated (21).

In 2019 during LHC Run 2, a 29-kg prototype detector for FASERν accumulated an integrated luminosity of 12.2 fb^{-1} at $\sqrt{s} = 13$ TeV (93). With lead and tungsten target plates and emulsion film interleaved and a fiducial volume that included 11 kg of target, a neutral vertex sample of events was collected. The dominant background to the neutral vertex events is from neutral hadrons produced by muons upstream that undergo inelastic scattering in the detector. The FASER Collaboration determined that their observations showed a 2.7σ excess of neutrino-like events over the backgrounds and demonstrated the principle of neutrino detection at the LHC (93).

New experiments in a proposed purpose-built Forward Physics Facility (FPF) would exploit the forward fluxes of neutrinos in the high-luminosity runs of the LHC (HL-LHC) (20, 21). Upgrades of FASERν to FASERν2 and of AdvSND (SND@LHC to Advanced SND), plus the addition of a liquid argon time projection chamber called FLArE, would be stationed in this new facility positioned ∼620–685 m from the ATLAS interaction point. With an integrated luminosity of 3,000 fb^{-1} and larger detectors, $\sim 10^6$ neutrino interactions, including $\sim 10^3$ tau neutrinos, are projected (21). With such a large flux of neutrinos, nuclear effects in neutrino scattering in detectors can be studied. It may be possible to detect trident events in the TeV energy range. The expected CC σ/E precision for a 10-ton detector with a 1 m × 1 m cross-sectional area at the FPF is shown in **Figure 4** for each flavor. Charge separation will be possible for muon and tau

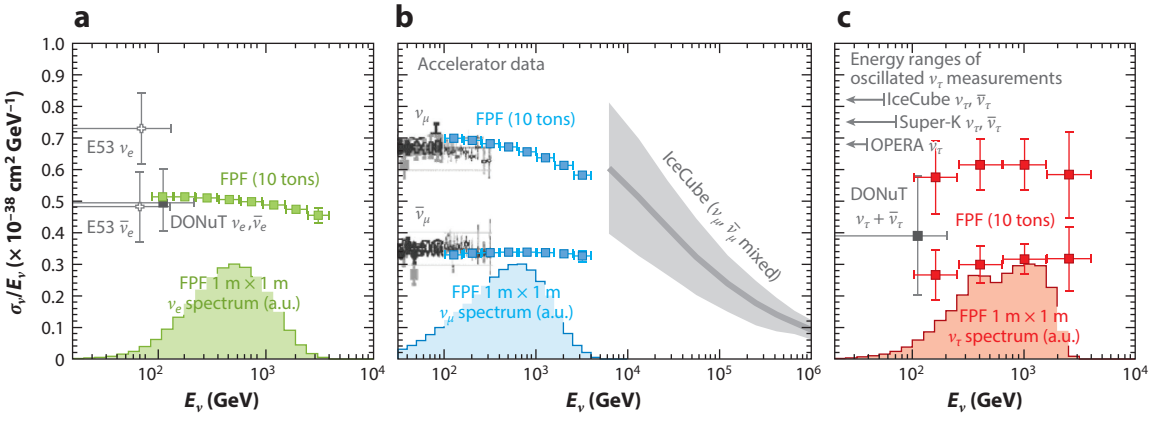

Figure 4

Projected precision of the (*a*) average $\nu_e + \bar{\nu}_e$ charged-current cross section with nucleons divided by energy and the separate (*b*) ν_μ and $\bar{\nu}_\mu$ and (*c*) ν_τ and $\bar{\nu}_\tau$ σ/E including statistical errors for a 10-ton neutrino detector at the Forward Physics Facility (FPF). Also shown are cross-section measurements from neutrino accelerator beam experiments (6) and the IceCube cross-section measurement using tracks (77). The shapes of the neutrino spectrum for a 1 m × 1 m detector at the FPF are shown as well. Figure adapted from Reference 21 (CC BY 4.0).

neutrinos and antineutrinos. Also shown in the figure are accelerator measurements (6) and the IceCube measurement using tracks (77). The HL-LHC schedule begins in 2029. Installation of FPF neutrino detectors would occur during the first run of the high-luminosity era.

5. THEORY AND SIMULATIONS OF NEUTRINO INTERACTIONS WITH $E > 10$ PeV

5.1. Small-x

As Equation 14 shows, at UHE the range of x extends to very low values—much lower than the range of x measured in hadron–hadron and lepton–hadron experiments. At very low x values, in addition to the higher-order QCD corrections associated with collinear logarithms discussed in Section 2.4, there are generically logarithms $\ln(1/x)$ that multiply the strong coupling constant. A resummation of powers $\alpha_s \ln(1/x)$ is performed with the Balitsky–Fadin–Kuraev–Lipatov (BFKL) framework (94, 95). A consistent resummation of both small-x and collinear logarithms through a combined BFKL and DGLAP formalism has been performed. The BGR18 neutrino cross sections (37, 59) come from evaluations at NNLO that also include the resummation at next-to-leading logarithmic accuracy in $\ln(1/x)$ (NLLx) with the NNPDF3.1sx + LHCb PDFs. The ratio of the BGR18 central cross section for neutrino CC scattering to the NLO evaluation using the CT18 NLO PDFs is shown in the inset to **Figure 2**. The uncertainty band shows the PDF uncertainty for the NNPDF3.1sx + LHCb PDF set (37). The deviation of the ratio from unity is small, and the narrow uncertainty band in the figure reflects both the availability of constraints from high-energy physics data (including from the LHCb experiment) and the stability of the structure functions to higher-order corrections.

The quark distribution functions at small x come from the sea—namely, from $g \to q\bar{q}$—so even in an LO evaluation of the neutrino cross section, the gluon PDF has an impact on the high-energy cross section. When the gluon density becomes very large at small x, the gluon density can saturate because the recombination $gg \to g$ introduces a nonlinear term to the DGLAP evolution of the PDFs. Gluon saturation would slow the growth of the cross section at UHE, a growth that would eventually lead to the violation of unitarity. Precisely where the onset of gluon saturation occurs is an open question, and indeed, it should depend not only on x but also on Q^2. The Balitsky–Kovchegov (BK) equation includes both $\ln(1/x)$ resummation and nonlinear corrections. It can be implemented through the dipole formalism and applied to the UHE cross section (46, 96). In Reference 46, Albacete et al. provide total cross-section predictions using the running coupling evaluation of the BK equation. Their cross section, multiplied by 0.68 to rescale to the CC cross section (labeled Albacete15), is shown with error bands in **Figure 5**. Also shown in **Figure 5** are the central values and uncertainty band for the NNLO + NLLx evaluation of σ_{CC}, labeled BGR18 (37).

Also displayed in **Figure 5** are CC cross sections from References 97 and 98. In Reference 97, the electromagnetic structure function F_2 is parameterized with a form that ensures that it scales as $\ln^2 s$ in the high-energy limit, as $x \to 0$ with Q^2 fixed. This asymptotic form respects the Froissart bound that comes from unitarity considerations. The bounds should also apply to the weak structure functions. The adaptation to neutrino scattering structure functions leads to the curve in **Figure 5** labeled Block14. This same structure function F_2 can be translated to a dipole cross section (99, 100), which in the dipole framework is used to evaluate the neutrino CC cross section labeled Argüelles15 in **Figure 5** (98).

The CC neutrino–nucleon cross-section predictions span a factor of ∼2 at the highest energies, which is not represented by the uncertainties in the PDF framework with or without NLLx contributions. Measurements of the neutrino cross section at UHE where predictions diverge will

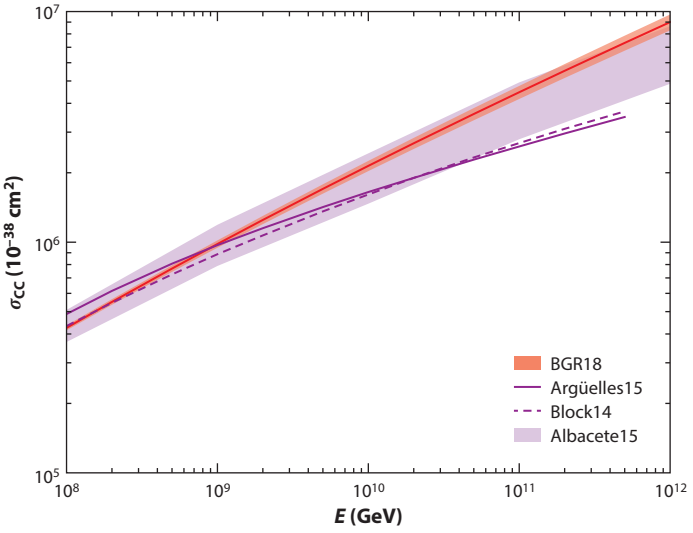

Figure 5

The charged-current cross section for neutrino scattering with isoscalar nucleons from Bertone, Gauld & Rojo (BGR18) with uncertainty band (37), a dipole model evaluation of the total cross section scaled by 0.68 to yield the charged-current cross section (Albacete15) (46), and cross sections from Block et al. (97) and Argüelles et al. (98).

shed light on the small-x structure functions, which could have implications for other high-energy physics processes in lepton–hadron and hadron–hadron interactions.

5.2. Beyond–Standard Model Physics with Neutrino Interactions

High-energy neutrinos can serve as probes of BSM interactions if BSM effects are manifest in distortions of the astrophysical neutrino spectrum and/or neutrino flavor ratios (101). In addition, BSM physics can be probed by UHE neutrino interactions with nucleons (102). The center-of-mass energy of the LHC of $\sqrt{s} = 13.6$ TeV corresponds to a neutrino energy of $E \simeq 100$ PeV incident on a fixed-target nucleon. At higher energies, neutrino interactions may exceed thresholds for new particles such as leptoquarks (103), or they may produce microscopic black holes that would signal large extra space-time dimensions (104). Enhanced cross sections from BSM physics would change neutrino flux attenuation in the Earth and affect event rates in neutrino telescopes. BSM physics can modify the Standard Model inelasticity distributions; thus, analyses beyond rescaling Standard Model cross-section results may be required (105).

Two anomalous events (106, 107) with energies ∼500 PeV have been observed by the balloon-borne Antarctic Impulsive Transient Antenna (ANITA), a neutrino telescope described in Section 6.2. The events have characteristics that suggest an origin of tau neutrino interactions in the Earth that produce taus that decay to yield upgoing air showers. Earth-skimming tau neutrinos are promising for detection of UHE neutrinos (108). However, the elevation angles of the ANITA showers are inconsistent with this interpretation because of neutrino flux attenuation in the Earth (109, 110). Currently unresolved, the ANITA events have motivated BSM explanations and demonstrate how UHE neutrino observations can test our understanding of the Standard Model.

5.3. Simulations of Neutrinos in the Earth

Because of the importance of neutrino attenuation in the Earth and CC production of muons and taus that enter an underground detector or emerge from the Earth for detection via air

showers, several groups have developed simulation codes for neutrino and charged-lepton propagation in the Earth. Available codes include nuPyProp (105), NuTauSim (111), TauRunner (112), NuPropEarth (59), and Danton (113).

For high-energy neutrino propagation in the Earth, the neutrino flavor is important. A special feature of ν_τ propagation in the Earth is neutrino regeneration (114). Tau neutrino CC interactions in the Earth attenuate the tau neutrino flux; however, the taus they produce decay to regenerate tau neutrinos at lower energies. Important elements are the short tau lifetime and the relatively low energy loss of the tau as it propagates in the Earth before it decays. Muon neutrinos are also regenerated in muon neutrino CC interactions followed by muon decays, but the very long muon lifetime and muon energy loss in transit mean that the regenerated muon neutrinos are at low energies. There are muon neutrinos that are regenerated from tau decays, which may be of interest for neutrino detection for UHE (115). Each of the simulation codes accounts for neutrino CC and NC interactions, charged-lepton energy loss, and tau neutrino regeneration. The TauRunner, NuPropEarth, and Danton codes include neutrinos of all flavors regenerated in tau decays. Simulations better represent neutrino flux attenuation than the schematic factor $\sim\exp[-X(\theta_z)/L_\nu(E)]$ discussed in Section 4.1.

Implementations in these codes differ in some of the details of cross sections, energy loss, and decays, but quantitatively, a comparison of results from the different codes shows good agreement. At the highest energies, the subleading contributions to UHE neutrino scattering in NuPropEarth account for some differences in predictions. A summary of the features of the codes and a comparison of the probabilities for ν_τ to produce taus that exit the Earth, as a function of energy and angle, appear in Reference 19.

6. PROSPECTS FOR MEASUREMENTS WITH $E > 10$ PeV

6.1. Ultrahigh-Energy Neutrinos in Astroparticle Physics

The diffuse astrophysical neutrino flux that has been measured by the IceCube Collaboration is expected to extend to UHE (see, e.g., 116, 117). Expected to come from multiple source categories, diffuse astrophysical neutrino models must satisfy observational constraints on the diffuse astrophysical electromagnetic spectrum and on the limits on correlated photon and neutrino signals from a given source (see, e.g., 118). In 2017, one neutrino event was observed from a direction coincident with a γ-ray blazar, TXS 0506+056 (119), opening an era of multimessenger astrophysics that includes neutrinos. More recently, the IceCube Collaboration reported a 79^{+22}_{-20} (4.2σ) excess of neutrino events associated with NGC 1068, a nearby active galaxy that is a possible steady source of neutrinos (120). Indeed, detection of transient and steady point sources of neutrinos is a goal of many current and future neutrino telescopes (121).

UHE neutrinos also come from high-energy cosmic ray interactions with the cosmic background radiation as cosmic rays travel over astronomical distances (122, 123). For cosmic ray protons, the process $p\gamma \rightarrow \Delta^+$ strongly attenuates the proton flux above proton energies of $\sim 5 \times 10^{10}$ GeV. This mechanism for the steep decline in the UHE cosmic ray spectrum (124, 125) is called the Greisen–Zatsepin–Kuzmin (GZK) cutoff. The high-energy cosmic ray spectrum shows a cutoff consistent with the GZK prediction (126, 127).

Neutrinos come from $p\gamma \rightarrow \Delta^+ \rightarrow \pi^+ n$. The charged-pion decay and subsequent muon decay and neutron decay all yield neutrinos. Theoretical predictions of this cosmogenic neutrino flux depend on quantities such as the maximum cosmic accelerator energy, the cosmic ray spectrum at the source, the mass composition of the UHE cosmic rays, and the evolution of sources of UHE cosmic rays (128, 129). There is a significant range of predictions of the cosmogenic neutrino flux because of the uncertainties in the inputs. In particular, if the highest-energy cosmic rays are

composed of heavy nuclei, the cosmic ray energies are increased by a factor of the mass number to reach the threshold for Δ^+ production. Thus far, neutrinos with energies above a few PeV have not been detected. The most stringent limits on the flux of neutrinos in the energy range of ~1 EeV come from IceCube (130) and the Pierre Auger Observatory (131), a cosmic ray observatory that searches for neutrino events in inclined showers and in showers from Earth-skimming tau neutrinos.

6.2. Neutrino Detection for $E > 10$ PeV

A feature of all flux predictions of very-high-energy and UHE neutrinos is that the fluxes decrease as a function of energy, a decrease that is faster than the slow rise of the neutrino cross section. Detection of neutrinos in this energy range requires even larger detectors or detection strategies to take advantage of large target volumes for incident neutrinos. Surveys of current and planned detectors for $E \gtrsim 1$–10 PeV appear in References 18 and 121. Table 1 of Reference 121 summarizes energy thresholds, angular resolutions, and other detector characteristics of current and future neutrino observatories. A brief review of detection methods for the relevant energy ranges is presented here.

Energy thresholds for optical Cherenkov signals in ice and water are determined by the vertical and horizontal spacing of detector optical modules for a given high-energy neutrino observatory. Optical Cherenkov signal detection continues to be an important means of identifying neutrino-induced signals, as evident from the international efforts of IceCube, Baikal-GVD, KM3NeT, and P-ONE. The planned IceCube-Gen2 (132) will expand IceCube's optical Cherenkov detection volume to 8 km^3.

A number of experiments in operation and in development are designed to detect radio signals from neutrino interactions in ice via the Askaryan effect (133). As reviewed in Reference 134, Cherenkov radiation with radio frequencies is generated by short-lived clusters of charge excess on the scale of $\mathcal{O}$(0.1–1 m) that develop from the neutrino-induced showers. The charge excess travels faster than the speed of light in ice and generates a short radio Cherenkov pulse. The kilometer-scale attenuation length of the radio signal is an advantage in scaling to larger volumes relative to the optical Cherenkov detection, given the optical signal attenuation length of order 100 m.

Neutrino energy thresholds $\gtrsim$10 PeV characterize in-ice radio detection experiments. Those currently in operation include the ARIANNA experiment (135) and the Askaryan Radio Array (ARA) (136) in Antarctica. The Radio Neutrino Observatory in Greenland (RNO-G) experiment (137, 138) has installation in progress of a radio antenna array that will cover an area of 50 km^2. Planned for IceCube-Gen2 is an array of radio antennas that will cover ~500 km^2 (132).

The cascades induced in ice by cosmic rays and neutrinos can be detected by a radar echo method that is being developed for the Radar Echo Telescope (RET) (139). Shower cascades in ice reflect transmitting antenna radio signals that are detected in receivers. In the prototype designed to detect cosmic ray–induced cascades, radio transmitters and receivers are near the ice surface. RET's expected sensitivity is to a neutrino energy range of 10 to 100 PeV.

Upgoing air showers would signal neutrino interactions in the Earth. The neutrino energy thresholds vary for surface detectors designed to detect signals from Earth-skimming tau neutrinos that produce extensive air showers (EASs) from tau decays. Trinity, a telescope that uses optical Cherenkov signals from EASs, is designed to detect the showers that originate from tau neutrinos in the 1-PeV to 1-EeV energy range. Trinity is currently in the demonstrator phase (140). Antennas to detect radio signals that come from geomagnetic effects on electrons and positrons in EASs (141) have neutrino energy thresholds of tens of PeV. The Beamforming Elevated Array for Cosmic Neutrinos (BEACON) is a detector concept for radio detection of tau neutrino–sourced air showers that is also in the demonstration phase (142). Using a staged

approach, the Giant Radio Array for Neutrino Detection (GRAND) project aims to instrument a 200,000 km^2 area for detection of geomagnetic radio emission (143). Other instruments detect particles from the air showers. The Pierre Auger Observatory detects particles from EASs from neutrinos with energies above 100 PeV (131). The Tau Air Shower Mountain-Based Observatory (TAMBO) (144) proposes to detect particles from tau neutrino–induced air showers, targeting neutrinos in the energy range of 1 to 100 PeV.

Balloon- or satellite-based instruments survey a large area of the Earth's surface for upgoing EASs and for Askaryan radio emissions that refract out of the ice. The balloon-borne ANITA project and its successor Payload for Ultrahigh Energy Observations (PUEO) (145) target radio signals from neutrino interactions with energies $\gtrsim$100 PeV. The EUSO-SPB2 project has a Cherenkov telescope and fluorescence telescope that are in preparation for balloon launch (146). EUSO-SPB2 will demonstrate the Cherenkov technique from balloon altitudes in preparation for a satellite-based project like the Probe of Extreme Multi-Messenger Astrophysics (POEMMA) observatory (147), in which the fluorescence telescope would be sensitive to neutrino energies above ∼10 EeV and the Cherenkov telescope would be sensitive to energies above ∼10 PeV.

6.3. Neutrino Cross-Section Measurement Strategies for $E > 10$ PeV

As for $E = 1$ TeV–1 PeV, the angular distribution of neutrino events is a key to measuring the neutrino cross section for $E > 10$ PeV. A recent analysis of the potential for neutrino cross-section measurements in generic detectors was presented in Reference 148. Using the effect of neutrino flux attenuation as a function of angle that depends on $\sim\exp[-X(\theta_z)/L_\nu(E)]$, a detector angular resolution of $\Delta(\theta) \leq 1°$, and a neutrino energy uncertainty of $\Delta\log_{10}(E) < 1$, the estimated precision of a cross-section measurement was determined for cases in which 10–100 events per decade of energy are detected coming from a neutrino flux with a power-law spectrum. For the neutrino energy range of 10 to 100 PeV, with 10 events the cross section can be measured to within $\sim^{+65\%}_{-35\%}$, improving to $\sim^{+20\%}_{-15\%}$ for 100 events from neutrinos in the energy range (148). Because higher-energy neutrinos emerge from narrower angular ranges below the horizon than lower-energy neutrinos, for neutrino energies between 1 and 10 EeV, 10 events will yield an uncertainty that ranges from ∼0.6 to more than a factor of two around the Standard Model cross section. For 100 events in this energy bin, the estimated cross-section error is $\sim^{+25\%}_{-15\%}$ (148). An analysis of skimming tau neutrino events using the projected sensitivities of GRAND and POEMMA arrives at a similar conclusion: that the cross-section error on a measurement of 100 events for $E \sim 1$ EeV is about ±20% (149).

Figure 6 shows the IceCube-Gen2 Radio 10-year projected errors for the CC neutrino cross section as a function of energy (150), taking the BGR18 cross section for the Standard Model cross section (37). Detailed simulations of neutrino propagation in the Earth, of neutrino generation of radio signals in the ice, and of the radio detector response for a 500 km^2 projected instrumented area were performed with a range of cosmogenic, astrophysical source, and combined astrophysical source plus cosmogenic flux models. The three fluxes shown in **Figure 6** are a cosmogenic flux that has a corresponding cosmic ray flux fit to the Telescope Array result (135), a power-law diffuse astrophysical flux (75), and the flux of cosmogenic neutrinos generated by UHE cosmic rays from all active galactic nuclei (AGN) (117). Again, important for the analysis is the zenith angle reconstruction uncertainty, which is taken here to be 2°. The analysis used a shower energy resolution of 0.1 in $\log_{10}(E^{\rm reco}_{\rm shr}/E_{\rm shr})$ for reconstructed shower energy $E^{\rm reco}_{\rm shr}$. As the colored bands in **Figure 6** expand, they correspond to hundreds of, tens of, and a few neutrino-induced showers for shower energies between 10 PeV and 10 EeV (150). Also shown in **Figure 6** are accelerator neutrino beam measurements (6) and results from IceCube analyses (77, 78, 80).

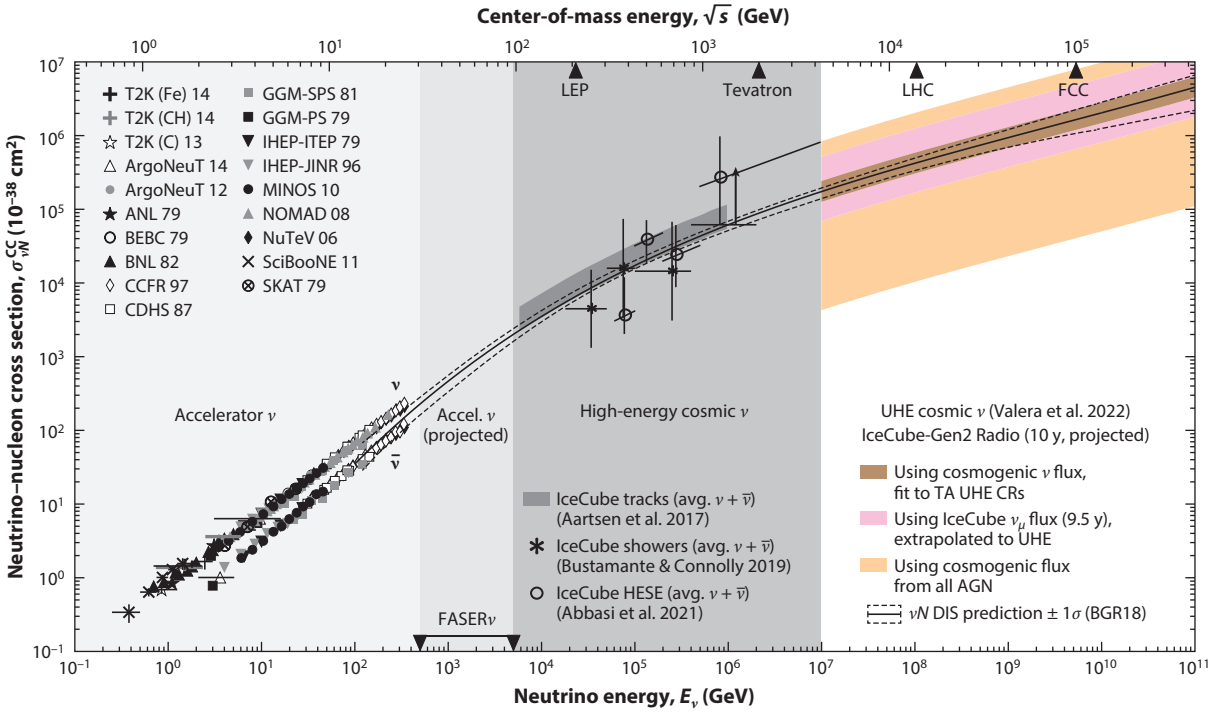

Figure 6

Predictions based on IceCube-Gen2 Radio (10 year, projected) of the UHE CC neutrino cross section as a function of energy (150). The colored error bands depend on the incoming neutrino flux: a cosmogenic flux based on a fit to Telescope Array UHE cosmic rays (152), an IceCube power-law spectrum extrapolated to UHE (75), and a cosmogenic flux from AGN from Rodrigues et al. (117). Shown are measurements from IceCube using muon tracks (77) and HESE (78) and from accelerator experiments (6). A separate determination (80) of the cross section from the IceCube shower sample is included in the figure. The BGR18 neutrino and antineutrino DIS cross sections with uncertainties are also shown (37). Abbreviations: AGN, active galactic nuclei; CC, charged current; CR, cosmic ray; DIS, deep inelastic scattering; FCC, Future Circular Collider; HESE, high-energy starting event; LEP, Large Electron–Positron Collider; LHC, Large Hadron Collider; TA, Telescope Array; UHE, ultrahigh-energy. Figure adapted from Reference 150 (CC BY 4.0).

The projections summarized here rely on cross sections that are Standard Model–like: The Standard Model cross sections are simply rescaled over a decade or more of energy, and the inelasticity distributions are simulated according to the Standard Model. If BSM physics is important in UHE neutrino interactions, cross-section error estimates will be revisited.

7. SUMMARY

Structure functions in DIS with nucleons describe neutrino and antineutrino differential scattering cross sections. The neutrino cross section in the energy region of ∼10 TeV to 1 PeV has been measured by IceCube. As ice and water Cherenkov detectors expand to larger volumes, the energy range of the cross-section measurements will increase as will the number of events. In addition, an FPF with neutrino detectors that capture the forward fluxes of neutrinos from proton–proton collisions at the LHC would extend accelerator neutrino beam cross-section measurements and fill in the energy gap between accelerator results and the IceCube results. High-statistics measurements would permit studies of nuclear effects and perhaps subleading contributions to the cross sections.

The UHE neutrino flux falls as neutrino energies increase, and there is a range of neutrino flux predictions. This makes cross-section measurements more difficult. With 100 events in the 1- to 10-EeV range, neutrino cross sections can be determined with an uncertainty that can start to distinguish between different approaches to the small-x treatment of the weak structure functions. It is likely that in the EeV neutrino energy range, a combination of all of the neutrino experiments and detection techniques will be needed for a combination of downward-going, upward-going and nearly horizontal (skimming) neutrino events. With enough events, it will be possible to unravel the separate effects of the neutrino flux and the neutrino cross section.

DISCLOSURE STATEMENT

The author is not aware of any affiliations, memberships, funding, or financial holdings that might be perceived as affecting the objectivity of this review.

ACKNOWLEDGMENTS

The author acknowledges I. Sarcevic, C. Quigg, R. Gandhi, and Y.S. Jeong for their contributions to her understanding of ultrahigh-energy neutrino interactions. The author thanks B. Zhou, F. Kling, V. Valera, and M. Bustamante for providing figures for this review. This work is supported in part by the US Department of Energy (grant DE-SC-0010113).

LITERATURE CITED

1. Vitagliano E, Tamborra I, Raffelt G. *Rev. Mod. Phys.* 92:45006 (2020)
2. Gonzalez-Garcia MC, Maltoni M. *Phys. Rep.* 460:1 (2008)
3. Engel K, Lewis T, Muzio MS, Venters TM. arXiv:2203.10074 [astro-ph.HE] (2022)
4. Formaggio JA, Zeller GP. *Rev. Mod. Phys.* 84:1307 (2012)
5. Sajjad Athar M, Fatima A, Singh SK. *Prog. Part. Nucl. Phys.* 129:104019 (2023)
6. Workman RL. (Part. Data Group.) *Prog. Theor. Exp. Phys.* 2022:083C01 (2022)
7. Kodama K, et al. (DONuT Collab.) *Phys. Lett. B* 504:218 (2001)
8. Kodama K, et al. (DONuT Collab.) *Phys. Rev. D* 78:052002 (2008)
9. Agafonova N, et al. (OPERA Collab.) *Phys. Lett. B* 691:138 (2010)
10. Agafonova N, et al. (OPERA Collab.) *Phys. Rev. Lett.* 120:211801 (2018). Erratum. *Phys. Rev. Lett.* 121:139901 (2018)
11. Gaisser TK, Honda M. *Annu. Rev. Nucl. Part. Sci.* 52:153 (2002)
12. Wolfenstein L. *Phys. Rev. D* 17:2369 (1978)
13. Fukuda S, et al. (Super-Kamiokande Collab.) *Phys. Rev. Lett.* 86:5656 (2001)
14. Ahmad QR, et al. (SNO Collab.) *Phys. Rev. Lett.* 89:011301 (2002)
15. Learned JG, Pakvasa S. *Astropart. Phys.* 3:267 (1995)
16. Beacom JF, et al. *Phys. Rev. D* 68:093005 (2003). Erratum. *Phys. Rev. D* 72:019901 (2005)
17. Bustamante M, Beacom JF, Winter W. *Phys. Rev. Lett.* 115:161302 (2015)
18. Ackermann M, et al. *J. High Energy Astrophys.* 36:55 (2022)
19. Abraham RM, et al. *J. Phys. G* 49:110501 (2022)
20. Anchordoqui LA, et al. *Phys. Rep.* 968:1 (2022)
21. Feng JL, et al. *J. Phys. G* 50:030501 (2023)
22. Albright CH, Jarlskog C. *Nucl. Phys. B* 84:467 (1975)
23. Kretzer S, Reno MH. *Phys. Rev. D* 69:034002 (2004)
24. Devenish R, Cooper-Sarkar A. *Deep Inelastic Scattering*. Oxford, UK/New York: Oxford Univ. Press (2004)
25. Jeong YS, Reno MH. *Phys. Rev. D* 82:033010 (2010)
26. Friedman JI. *Rev. Mod. Phys.* 63:615 (1991)
27. Kendall HW. *Rev. Mod. Phys.* 63:597 (1991)

28. Taylor RE. *Rev. Mod. Phys.* 63:573 (1991)
29. Brock R, et al. *Rev. Mod. Phys.* 67:157 (1995)
30. Gribov VN, Lipatov LN. *Sov. J. Nucl. Phys.* 15:438 (1972)
31. Dokshitzer YL. *Sov. Phys. JETP* 46:641 (1977)
32. Altarelli G, Parisi G. *Nucl. Phys. B* 126:298 (1977)
33. Gao J, Harland-Lang L, Rojo J. *Phys. Rep.* 742:1 (2018)
34. Ethier JJ, Nocera ER. *Annu. Rev. Nucl. Part. Sci.* 70:43 (2020)
35. Gandhi R, Quigg C, Reno MH, Sarcevic I. *Astropart. Phys.* 5:81 (1996)
36. Gandhi R, Quigg C, Reno MH, Sarcevic I. *Phys. Rev. D* 58:093009 (1998)
37. Bertone V, Gauld R, Rojo J. *J. High Energy Phys.* 1901:217 (2019)
38. Bardeen WA, Buras AJ, Duke DW, Muta T. *Phys. Rev. D* 18:3998 (1978)
39. Altarelli G, Ellis RK, Martinelli G. *Nucl. Phys. B* 157:461 (1979)
40. Furmanski W, Petronzio R. *Z. Phys. C* 11:293 (1982)
41. Zijlstra EB, van Neerven WL. *Phys. Lett. B* 297:377 (1992)
42. Zijlstra EB, van Neerven WL. *Nucl. Phys. B* 383:525 (1992)
43. Moch S, Vermaseren JAM, Vogt A. *Nucl. Phys. B* 688:101 (2004)
44. Vogt A, Moch S, Vermaseren JAM. *Nucl. Phys. B* 691:129 (2004)
45. Buckley A, et al. *Eur. Phys. J. C* 75:132 (2015)
46. Albacete JL, Illana JI, Soto-Ontoso A. *Phys. Rev. D* 92:014027 (2015)
47. Jeong YS, Reno MH. *Phys. Rev. D* 81:114012 (2010)
48. Connolly A, Thorne RS, Waters D. *Phys. Rev. D* 83:113009 (2011)
49. Cooper-Sarkar A, Mertsch P, Sarkar S. *J. High Energy Phys.* 1108:42 (2011)
50. Hou TJ, et al. *Phys. Rev. D* 103:014013 (2021)
51. Cooper-Sarkar A. arXiv:1012.1438 [hep-ph] (2010)
52. Gottschalk T. *Phys. Rev. D* 23:56 (1981)
53. Aivazis MAG, Olness FI, Tung WK. *Phys. Rev. D* 50:3085 (1994)
54. Aivazis MAG, Collins JC, Olness FI, Tung WK. *Phys. Rev. D* 50:3102 (1994)
55. Thorne RS, Roberts RG. *Phys. Rev. D* 57:6871 (1998)
56. Thorne RS. *Phys. Rev. D* 86:074017 (2012)
57. Bertone V, et al. *Eur. Phys. J. C* 77:837 (2017)
58. Barnett RM. *Phys. Rev. Lett.* 36:1163 (1976)
59. Garcia A, Gauld R, Heijboer A, Rojo J. *J. Cosmol. Astropart. Phys.* 2009:025 (2020)
60. Kovarik K, et al. *Phys. Rev. D* 93:085037 (2016)
61. Eskola KJ, Paakkinen P, Paukkunen H, Salgado CA. *Eur. Phys. J. C* 77:163 (2017)
62. Kopeliovich BZ, Morfin JG, Schmidt I. *Prog. Part. Nucl. Phys.* 68:314 (2013)
63. Armesto N. *J. Phys. G* 32:R367 (2006)
64. Aubert JJ, et al. *Phys. Lett. B* 123:275 (1983)
65. Geesaman DF, Saito K, Thomas AW. *Annu. Rev. Nucl. Part. Sci.* 45:337 (1995)
66. Klein SR, Robertson SA, Vogt R. *Phys. Rev. C* 102:015808 (2020)
67. Glashow SL. *Phys. Rev.* 118:316 (1960)
68. Gauld R. *Phys. Rev. D* 100:091301 (2019)
69. Aartsen MG, et al. (IceCube Collab.) *Nature* 591:220 (2021). Erratum. *Nature* 592:E11 (2021)
70. Seckel D. *Phys. Rev. Lett.* 80:900 (1998)
71. Alikhanov I. *Phys. Lett. B* 756:247 (2016)
72. Zhou B, Beacom JF. *Phys. Rev. D* 101:036011 (2020)
73. Waxman E, Bahcall JN. *Phys. Rev. D* 59:023002 (1999)
74. Aartsen MG, et al. (IceCube Collab.) *J. Instrum.* 12:P03012 (2017)
75. Abbasi R, et al. (IceCube Collab.) *Astrophys. J.* 928:50 (2022)
76. Abbasi R, et al. (IceCube Collab.) *Phys. Rev. D* 104:022002 (2021)
77. Aartsen MG, et al. (IceCube Collab.) *Nature* 551:596 (2017)
78. Abbasi R, et al. (IceCube Collab.) *Phys. Rev. D* 104:022001 (2021)
79. Abbasi R, et al. (IceCube Collab.) *Proc. Sci.* ICRC2021:1158 (2021)

80. Bustamante M, Connolly A. *Phys. Rev. Lett.* 122:041101 (2019)
81. Gonçalves VP, Gratieri DR, Quadros ASC. *Eur. Phys. J. C* 82:1011 (2022)
82. Aartsen MG, et al. (IceCube Collab.) *Phys. Rev. D* 99:032004 (2019)
83. Adrian-Martinez S, et al. (KM3Net Collab.) *J. Phys. G* 43:084001 (2016)
84. Ageron M, et al. (ANTARES Collab.) *Nucl. Instrum. Meth. A* 656:11 (2011)
85. Allakhverdyan VA, et al. *Phys. At. Nucl.* 84:1600 (2021)
86. Agostini M, et al. (P-ONE Collab.) *Nat. Astron.* 4:913 (2020)
87. Resconi E. *Proc. Sci.* ICRC2021:024 (2022)
88. Bhattacharya A, Gandhi R, Rodejohann W, Watanabe A. *J. Cosmol. Astropart. Phys.* 1110:017 (2011)
89. De Rujula A, Ruckl R. In *Proceedings of the ECFA-CERN Workshop on Large Hadron Collider in the LEP Tunnel*, ed. M Jacob, pp. 571–96. Geneva: CERN (1984)
90. De Rujula A, Fernandez E, Gomez-Cadenas JJ. *Nucl. Phys. B* 405:80 (1993)
91. Abreu H, et al. (FASER Collab.) arXiv:2207.11427 [physics.ins-det] (2022)
92. Acampora G, et al. (SND@LHC Collab.) arXiv:2210.02784 [hep-ex] (2022)
93. Abreu H, et al. (FASER Collab.) *Phys. Rev. D* 104:L091101 (2021)
94. Kuraev EA, Lipatov LN, Fadin VS. *Sov. Phys. JETP* 45:199 (1977)
95. Balitsky II, Lipatov LN. *Sov. J. Nucl. Phys.* 28:822 (1978)
96. Gonçalves VP, Hepp P. *Phys. Rev. D* 83:014014 (2011)
97. Block MM, Durand L, Ha P. *Phys. Rev. D* 89:094027 (2014)
98. Argüelles CA, et al. *Phys. Rev. D* 92:074040 (2015)
99. Ewerz C, von Manteuffel A, Nachtmann O. *J. High Energy Phys.* 1103:62 (2011)
100. Jeong YS, Kim CS, Luu MV, Reno MH. *J. High Energy Phys.* 1411:25 (2014)
101. Adhikari RX, et al. arXiv:2209.11726 [hep-ph] (2022)
102. Ackermann M, et al. *Bull. Am. Astron. Soc.* 51:215 (2019)
103. Huang G-Y, Jana S, Lindner M, Rodejohann W. *J. Cosmol. Astropart. Phys.* 2202:038 (2022)
104. Alvarez-Muñiz J, Feng JL, Halzen F, Han T, Hooper D. *Phys. Rev. D* 65:124015 (2002)
105. Garg D, et al. *J. Cosmol. Astropart. Phys.* 2301:041 (2023)
106. Gorham PW, et al. (ANITA Collab.) *Phys. Rev. Lett.* 117:071101 (2016)
107. Gorham PW, et al. (ANITA Collab.) *Phys. Rev. Lett.* 121:161102 (2018)
108. Fargion D. *Astrophys. J.* 570:909 (2002)
109. Romero-Wolf A, et al. *Phys. Rev. D* 99:063011 (2019)
110. Chipman S, Diesing R, Reno MH, Sarcevic I. *Phys. Rev. D* 100:063011 (2019)
111. Alvarez-Muñiz J, et al. *Phys. Rev. D* 97:023021 (2018). Erratum. *Phys. Rev. D* 99:069902 (2019)
112. Safa I, et al. *Comput. Phys. Commun.* 278:108422 (2022)
113. Niess V, Martineau-Huynh O. arXiv:1810.01978 [physics.comp-ph] (2018)
114. Halzen F, Saltzberg D. *Phys. Rev. Lett.* 81:4305 (1998)
115. Argüelles CA, Halzen F, Kheirandish A, Safa I. arXiv:2203.13827 [astro-ph.HE] (2022)
116. Muzio MS, Farrar GR, Unger M. *Phys. Rev. D* 105:023022 (2022)
117. Rodrigues X, et al. *Phys. Rev. Lett.* 126:191101 (2021)
118. Palladino A, Rodrigues X, Gao S, Winter W. *Astrophys. J.* 871:41 (2019)
119. Aartsen MG, et al. *Science* 361:eaat1378 (2018)
120. Abbasi R, et al. (IceCube Collab.) *Science* 378:538 (2022)
121. Guépin C, Kotera K, Oikonomou F. *Nat. Rev. Phys.* 4:697 (2022)
122. Berezinsky V, Zatsepin G. *Phys. Lett. B* 28:423 (1969)
123. Stecker F. *Astrophys. J.* 228:919 (1979)
124. Greisen K. *Phys. Rev. Lett.* 16:748 (1966)
125. Zatsepin G, Kuzmin V. *JETP Lett.* 4:78 (1966)
126. Ivanov D. *Proc. Sci.* ICRC2019:298 (2020)
127. Abreu P, et al. (Pierre Auger Collab.) *Proc. Sci.* ICRC2021:324 (2021)
128. Kotera K, Allard D, Olinto AV. *J. Cosmol. Astropart. Phys.* 1010:013 (2010)
129. Aloisio R, et al. *J. Cosmol. Astropart. Phys.* 1510:006 (2015)
130. Aartsen MG, et al. (IceCube Collab.) *Phys. Rev. D* 98:062003 (2018)

131. Aab A, et al. (Pierre Auger Collab.) *J. Cosmol. Astropart. Phys.* 1910:022 (2019)
132. Aartsen MG, et al. (IceCube-Gen2 Collab.) *J. Phys. G* 48:060501 (2021)
133. Askar'yan GA. *Zh. Eksp. Teor. Fiz.* 41:616 (1961)
134. Barwick S, Glaser C. arXiv:2208.04971 [astro-ph.IM] (2022)
135. Anker A, et al. (ARIANNA Collab.) *Adv. Space Res.* 64:2595 (2019)
136. Allison P, et al. (ARA Collab.) *Phys. Rev. D* 105:122006 (2022)
137. Aguilar JA, et al. *Eur. Phys. J. C* 82:147 (2022)
138. Aguilar JA, et al. (RNO-G Collab.) *Proc. Sci.* ICRC2021:001 (2021)
139. Prohira S, et al. *Phys. Rev. D* 104:102006 (2021)
140. Brown AM, et al. *Proc. Sci.* ICRC2021:1179 (2021)
141. Scholten O, Werner K, Rusydi F. *Astropart. Phys.* 29:94 (2008)
142. Wissel S, et al. *J. Cosmol. Astropart. Phys.* 2011:065 (2020)
143. Alvarez-Muñiz J, et al. (GRAND Collab.) *Sci. China Phys. Mech. Astron.* 63:219501 (2020)
144. Romero-Wolf A, et al. arXiv:2002.06475 [astro-ph.IM] (2020)
145. Abarr Q, et al. (PUEO Collab.) *J. Instrum.* 16:P08035 (2021)
146. Adams JH, et al. arXiv:1703.04513 [astro-ph.HE] (2017)
147. Olinto AV, et al. (POEMMA Collab.) *J. Cosmol. Astropart. Phys.* 2106:007 (2021)
148. Esteban I, Prohira S, Beacom JF. *Phys. Rev. D* 106:023021 (2022)
149. Denton PB, Kini Y. *Phys. Rev. D* 102:123019 (2020)
150. Valera VB, Bustamante M, Glaser C. *J. High Energy Phys.* 2206:105 (2022)
151. Ball RD, et al. *Eur. Phys. J. C* 78:321 (2018)
152. Anker A, et al. arXiv:2004.09841 [astro-ph.IM] (2020)

Annual Review of Nuclear and Particle Science
Volume 73, 2023

Contents

Errata

An online log of corrections to *Annual Review of Nuclear and Particle Science* articles may be found at http://www.annualreviews.org/errata/nucl